Biophysical*Journal*
Article

Entropy Hotspots for the Binding of Intrinsically Disordered Ligands to a Receptor Domain

Jie Shi,[1] Qingliang Shen,[2] Jae-Hyun Cho,[2,*] and Wonmuk Hwang[1,3,4,5,*]
[1]Department of Biomedical Engineering, [2]Department of Biochemistry and Biophysics, [3]Department of Materials Science and Engineering, and [4]Department of Physics and Astronomy, Texas A&M University, College Station, Texas; and [5]School of Computational Sciences, Korea Institute for Advanced Study, Seoul, South Korea

ABSTRACT Proline-rich motifs (PRMs) are widely used for mediating protein-protein interactions with weak binding affinities. Because they are intrinsically disordered when unbound, conformational entropy plays a significant role for the binding. However, residue-level differences of the entropic contribution in the binding of different ligands remain not well understood. We use all-atom molecular dynamics simulation and the maximal information spanning tree formalism to analyze conformational entropy associated with the binding of two PRMs, one from the Abl kinase and the other from the nonstructural protein 1 of the 1918 Spanish influenza A virus, to the N-terminal SH3 (nSH3) domain of the CrkII protein. Side chains of the stably folded nSH3 experience more entropy change upon ligand binding than the backbone, whereas PRMs involve comparable but heterogeneous entropy changes among the backbone and side chains. In nSH3, two conserved nonpolar residues forming contacts with the PRM experience the largest side-chain entropy loss. In contrast, the C-terminal charged residues of PRMs that form polar contacts with nSH3 experience the greatest side-chain entropy loss, although their "fuzzy" nature is attributable to the backbone that remains relatively flexible. Thus, residues that form high-occupancy contacts between nSH3 and PRM do not reciprocally contribute to entropy loss. Furthermore, certain surface residues of nSH3 distal to the interface with PRMs gain entropy, indicating a nonlocal effect of ligand binding. Comparing between the PRMs from cAbl and nonstructural protein 1, the latter involves a larger side-chain entropy loss and forms more contacts with nSH3. Consistent with experiments, this indicates stronger binding of the viral ligand at the expense of losing the flexibility of side chains, whereas the backbone experiences less entropy loss. The entropy "hotspots" as identified in this study will be important for tuning the binding affinity of various ligands to a receptor.

SIGNIFICANCE Receptor-ligand binding relies not only on specific interactions between amino acids, but changes in the degrees of molecular flexibility upon binding, i.e., conformational entropy, are also critical. Our computational analysis identifies "entropy hotspot" residues that incur large entropy changes upon the binding of intrinsically disordered cellular and viral ligands to a protein receptor domain. These residues are located at the binding interface as well as away from the interface. Our results elucidate how the viral peptide binds to the receptor with a higher affinity, and our approach is applicable to the analysis and design of ligands binding to other target receptors.

INTRODUCTION

Intrinsically disordered proteins (IDP) or proteins containing intrinsically disordered regions (IDR) are abundant in cells (1), and they are widely involved in recognition between proteins (2–7). Many IDPs/IDRs undergo disorder-to-order transitions upon binding to their partner proteins. The high entropic penalty for disorder-to-order transition leads to a relatively low binding affinity (5,7,8), which may help with reversible signaling when quick turnover is desired (2,5,9). In systems with a higher binding affinity, the entropic penalty is offset by favorable enthalpy and/or it is reduced by retaining the "fuzziness" in the complexed state (3,7,8). Such fully or partially unstructured yet functional protein complexes have challenged the traditional notion of a lock-and-key binding mechanism involving well-defined structural states (1).

The proline-rich motif (PRM) is one of the most abundant linear motifs found in IDPs/IDRs (10,11). The cyclic structure of proline limits conformational degrees of freedom (DOFs) (12), and PRMs tend to form left-handed polyproline type II (PPII) helices upon binding to its receptor (13). In a PPII helix, backbone carbonyl and side-chain groups are exposed and can form intermolecular contacts

---

Submitted November 8, 2019, and accepted for publication March 23, 2020.

*Correspondence: jaehyuncho@tamu.edu or hwm@tamu.edu

Editor: Amedeo Caflisch.
https://doi.org/10.1016/j.bpj.2020.03.026

(12). This makes PRMs as common recognition motifs for many signaling proteins such as Src homology 3 (SH3) and WW domains (10,11,14,15). The binding generally involves negative (favorable) enthalpy and negative (unfavorable) entropy changes (6,8,16); the latter is due to the PPII helix formation upon binding (8,17–19).

Despite the importance of conformational entropy for binding, residue-level contribution has been difficult to quantify. Previous analysis considered mainly changes in the backbone conformation, whereas less is known about specific contributions of side chains (8). Experimentally, the "entropy meter" approach that empirically relates NMR-derived order parameters of side-chain methyl groups to entropy has been effective (20–24), but it is difficult to apply to proteins with a low content of methyl-bearing amino acids such as SH3 and its ligands. On the other hand, various computational methods have been developed for calculating conformational entropy. Early efforts included normal mode analysis (NMA) (25–27) and direct enumeration of side-chain rotamers (28,29). However, NMA cannot account for transitions between energy minima because it relies on an harmonic approximation of the potential energy surface about a single energy minimum. The direct enumeration approach becomes prohibitive for large proteins. NMA has also been applied to different snapshots of a molecular dynamics (MD) simulation trajectory. This mitigates the problem of working only around a single energy minimum, and it has been used for the study of ligand binding to SH3 domains (30,31). However, the computational cost of NMA limited the number of coordinate frames used, which likely resulted in only a small contribution of entropy to the binding specificity of different ligands (31). These limitations were partly addressed by a Monte Carlo simulation of side chains while the protein backbone was held fixed (32). It yielded total side-chain entropies among various systems correlating well with experimental values. Despite much insight this study provided, because of the simplified interaction potential that was introduced to allow Monte Carlo moves and because of the backbone being fixed to the crystallographic conformation, the accuracy and applicability of the method were limited when comparing entropy changes in the binding of different ligands or for finding residue-level contributions to entropy.

The above suggests that detailed residue-level analysis of the entropy of ligand binding based on unbiased atomistic MD simulation has been difficult. To this end, we employ the maximal information spanning tree (MIST) approach (33,34). MIST is an approximation method that overcomes the difficulty of direct enumeration arising from the large number of DOFs in typical biomolecular systems. It first calculates entropies of individual DOFs and then it adds corrections arising from higher order correlated motions among DOFs in such a way that the estimated entropy monotonically approaches the exact value as higher order correlations are accounted for. MIST yielded results that agree well with experimental estimates based on the entropy meter approach for several different systems (20). We apply MIST to study the binding between two PRMs and an SH3 domain. We use the N-terminal SH3 (nSH3) domain of a signaling adaptor protein CrkII (35,36). Among its various ligands (37,38), we used PRM$^{\mathrm{cAbl}}$ and PRM$^{\mathrm{NS1}}$ (Fig. 1). PRM$^{\mathrm{cAbl}}$ is from the C-terminal disordered region of the cAbl protein (35,39,40). PRM$^{\mathrm{NS1}}$ is from the C-terminal tail of the nonstructural protein 1 (NS1) of the 1918 Spanish influenza A virus (41,42). Upon binding to CrkII with high affinity, NS1 inhibits CrkII's interaction with other proteins including cAbl, thereby suppressing the host cell's immune response (41–43). Our earlier study has shown that PRM$^{\mathrm{NS1}}$ retains conformational flexibility even after binding to the nSH3 domain (44). This prompts the potential difference of entropy associated with the binding of the viral PRM$^{\mathrm{NS1}}$ and the cellular PRM$^{\mathrm{cAbl}}$ ligands.

We carry out MD simulations of different nSH3:PRM systems either in a complex or in isolation. A 500-ns simulation for each system yielded convergence of the backbone amide bond order parameter and conformational entropy. By using the MIST method, we found that side chains are mainly responsible for entropy changes in the stably folded nSH3, whereas for PRM that form a PPII helix upon binding, both backbone and side chains contribute comparably to entropy changes. Analysis of per-residue entropy and intermolecular contacts yielded residues that incur large side-chain entropy changes upon binding (i.e., entropy hotspots). We found nonreciprocal contributions of the entropy hotspot residues forming contacts at the nSH3:PRM interface as well as the long-range effect of ligand binding, which increases entropies of residues distal to the interface. Comparing between PRM$^{\mathrm{NS1}}$ and PRM$^{\mathrm{cAbl}}$, the former involves greater overall entropy loss and also forms a larger number of high-occupancy contacts with nSH3, which suggests a stronger and more rigid binding of the influenza peptide, consistent with its stronger binding affinity (40,43). Given that NS1 is a high-priority target for developing anti-influenza compounds (45) and with the diversity of the SH3 domain and its ligands (14,37,38,46), this approach elucidating the residue-specific entropy contributions will be of practical utility as well as being applicable to studies of other protein-protein interactions in general.

METHODS

Structures used

We used six simulation systems as follows:

1) nSH3:PRM$^{\mathrm{cAbl}}$: Protein Data Bank (PDB) code 5IH2 (1.8-Å resolution) (40);
2) nSH3:PRM$^{\mathrm{NS1A}}$: PDB 5UL6 (1.45 Å) (43);
3) nSH3:PRM$^{\mathrm{NS1B}}$: PDB 6ATV (1.75 Å) (43);
4) nSH3: Isolated from nSH3:PRM$^{\mathrm{cAbl}}$;
5) PRM$^{\mathrm{cAbl}}$: Isolated from nSH3:PRM$^{\mathrm{cAbl}}$; and

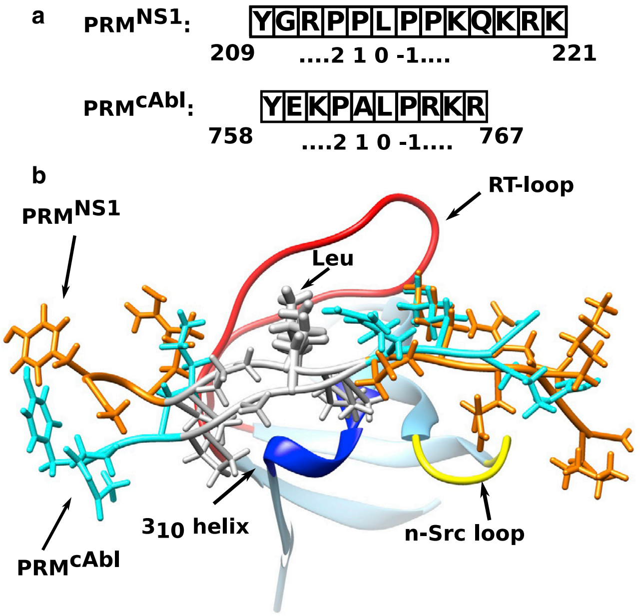

FIGURE 1 Structural overview of nSH3:PRM^{cAbl} and nSH3:PRM^{NS1}. (*a*) Sequences of the two ligands are shown. Relative positions are marked below, where the central Leu is at position 0. The position index increases N-terminally (40,43). (*b*) Two structures superimposed relative to the nSH3 domain are shown. PRM^{cAbl} and PRM^{NS1} are colored differently, and the central PxxP motif is white. Major subdomains of nSH3 (n-Src and RT loops, and 3_{10} helix) that interact with the PRM are shown in solid colors. The rest of nSH3 is semitransparent. To see this figure in color, go online.

6) PRM^{NS1}: Isolated from nSH3:PRM^{NS1B}.

Among the above, nSH3:PRM^{NS1A} and nSH3:PRM^{NS1B} are two different crystal structures of the nSH3:PRM^{NS1} complex, labeled in the same way as in our previous study (44).

Simulation

For simulation, we used CHARMM (47,48) with the param36 all-atom force field (49). Before solvation, a four-stage energy minimization was carried out. In each stage, backbone heavy atoms were harmonically restrained, and 100 steps of steepest descent followed by 300 steps of the adopted basis Newton-Raphson minimization were performed. The stiffness of the harmonic restraint was, in kcal/mol•Å^2 units, 5 (stage 1), 1 (stage 2), 0.1 (stage 3), and 0 (stage 4; no restraint). The system was solvated in a cubic TIP3P water box (50) of a side length of ~60 Å (nSH3:PRM), 56 Å (nSH3 only), and 54 Å (PRM only). Ions (Cl$^-$ and Na$^+$) were added to neutralize the system at ~150-mM concentration. Simulation systems had ~21,000 (nSH3:PRM), 16,000 (nSH3 only), and 15,000 (PRM only) atoms.

After solvation, the four-stage energy minimization explained above was applied again for the protein. The system was heated from 0 to 300 K over 100 ps followed by equilibration for 160 ps at 300 K. These were performed under a constant temperature and pressure (NPT) condition at 1 atm without any restraints. Each production run was under the constant volume and temperature (NVT) condition at 300 K for 500 ns. The integration step size was 2 fs. Lengths of covalent bonds involving hydrogen atoms were fixed by applying the SHAKE algorithm (51). The nonbonded interaction had a 12-Å cutoff. The particle-mesh Ewald summation method (52) was used to account for long-range electrostatic interactions under a periodic boundary condition. The Domain Decomposition (DOMDEC) module (53) of CHARMM was used to enhance parallel performance. Coordinates were saved every 5 ps. Visualization of structures were done using VMD (54) or UCSF Chimera (55). Calculations of root mean-square fluctuation (RMSF), order parameter, entropy, and contact occupancy were all based on the 100–500 ns interval to avoid the effect of the initial state. The 100-ns cutoff was determined by the relaxation times calculated for the angular reorientational correlation functions of the backbone amide N-H bonds, as explained below.

Order parameter

After aligning coordinate frames to the initial frame using backbone heavy atoms, we calculated the Lipari-Szabo squared generalized order parameter S^2 (56). Let $\vec{\mu}$ be the unit vector for the amide N-H bond with Cartesian components μ_i ($i = 1, 2, 3$). Then,

$$S^2 = \frac{1}{2}\left(3\sum_{i=1}^{3}\sum_{j=1}^{3}\left\langle \mu_i\mu_j\right\rangle^2 - 1\right), \tag{1}$$

where $\langle \cdot \rangle$ indicates the average over coordinate frames (57,58). To calculate S^2 for nSH3 or PRM within an nSH3:PRM complex, we aligned the backbone heavy atoms of the respective part to be consistent with the uncomplexed case. Statistical uncertainty was estimated by subsampling the trajectory every eighth frame and calculating the SD in S^2 from the eight subsamples. This method was more effective than using eight consecutive 50-ns intervals because relaxation times differ across the protein.

To assess the convergence of our trajectory, we calculated the angular reorientational correlation function $C_I(t)$ (57):

$$C_I(t) = \langle P_2(\vec{\mu}(\tau)\cdot\vec{\mu}(\tau+t))\rangle_\tau, \tag{2}$$

where $P_2(x) = (1/2)(3x^2 - 1)$ is the second Legendre polynomial. For each t, the average was taken over τ, ranging from 100 to $(500 - t)$ ns.

Order parameters were also estimated from NMR relaxation experiments, as described previously (44). Using Modelfree version 4.20 (59,60) and FAST-Modelfree softwares, R_1, R_2, and heteronuclear nuclear Overhauser effect were analyzed according to the Lipari-Szabo model-free formalism (56,61). An isotropic diffusion model was used for the analysis of the free nSH3 domain, and an axially symmetric model was used for nSH3:PRM complexes (8).

Entropy

We used backbone and side-chain rotation angles as DOFs: for backbone, ϕ and ψ angles (62), and for the side chain, the dihedral χ angles (63). Compared to bond lengths and bond angles, χ angles are the main contributors to the side-chain entropy (20,26,29). Angles were measured using the CORREL facility of CHARMM. For a coordinate trajectory, histograms of angles were constructed with a bin size $\Delta = 10°$. It is the smallest among bin sizes used previously, ranging from 10° (21) to 120° (20). Other choices, $\Delta = 8°$ and 15°, were also used as a test, but our main results did not depend on the precise choice of Δ. For a statistical uncertainty estimate, we subsampled the 100–500-ns interval every four frames and used the four sets, each containing the number of frames equal to 100 ns.

MIST

To calculate the conformational entropy using MIST (33,34), we started with the first order in which DOFs are treated independently. From the histogram of a given DOF, we built the normalized probability distribution function (PDF) $P(\alpha_m^i)$ (m: DOF index, i: bin index). The first-order MIST (MIST1) entropy is as follows:

$$S_1^{\mathrm{MIST}} = -k_B \Delta \sum_{m=1}^{\mathrm{DOF}} \sum_{i}^{\mathrm{Bin}} P\left(\alpha_m^i\right) \ln P\left(\alpha_m^i\right), \tag{3}$$

where k_B is the Boltzmann constant.

We used the joint PDF $P(\alpha_m^i, \alpha_n^j)$ to calculate the second-order mutual information between DOF m and n:

$$I_2(m;n) = \Delta^2 \sum_{i,j}^{\mathrm{Bin}} P\left(\alpha_m^i, \alpha_n^j\right) \ln \frac{P\left(\alpha_m^i, \alpha_n^j\right)}{P\left(\alpha_m^i\right) P\left(\alpha_n^j\right)} \tag{4}$$

The second-order MIST (MIST2) entropy is calculated by including I_2 for one DOF at a time, in which only the maximal I_2 between the current DOF and all previously added DOFs is included:

$$S_2^{\mathrm{MIST}} = S_1^{\mathrm{MIST}} - k_B \sum_{p=2}^{\mathrm{DOF}} \max_{q \in \{1,\ldots,(p-1)\}} [I_2(p;q)] \tag{5}$$

The third-order MIST (MIST3) is calculated similarly, by evaluating the third-order mutual information between DOF p and a pair of DOFs $\{q, r\}$:

$$I_3(p;q,r) = \Delta^3 \sum_{i,j,k}^{\mathrm{Bin}} P\left(\alpha_p^i, \alpha_q^j, \alpha_r^k\right) \ln \frac{P\left(\alpha_p^i, \alpha_q^j, \alpha_r^k\right)}{P\left(\alpha_p^i\right) P\left(\alpha_q^j, \alpha_r^k\right)}, \tag{6}$$

so that,

$$S_3^{\mathrm{MIST}} = S_1^{\mathrm{MIST}} - k_B \sum_{p=3}^{\mathrm{DOF}} \max_{\{q,r\} < p,\ q \neq r} [I_3(p;q,r)] \tag{7}$$

For a given p, only the maximal I_3 from all pairs of DOFs with indices less than p is included in the sum. If a certain DOF r is statistically independent of p and q, Eq. 6 becomes identical to Eq. 4. So Eq. 7 includes pairwise correlations for MIST2. In principle, higher order MIST can yield a more accurate (and smaller) estimation of entropy. But without a strong multivariate correlation, the improvement is marginal, whereas the computational cost steeply rises, and the high-dimensional joint PDF becomes less accurate because of the limited sample size. Thus, calculations up to the second or third order are practical (20,22).

For nSH3, we excluded the first A134 and the last R191 from entropy calculation, as done previously (40). We also excluded the terminal residues of PRMs (8). The number of DOFs were 235 for nSH3, 59 for PRM$^{\mathrm{NS1}}$, and 45 for PRM$^{\mathrm{cAbl}}$. Entropies were calculated using custom-written R language scripts and also using FORTRAN 95 codes parallelized with OpenMP.

Entropy per residue

The backbone entropy of each residue was calculated using the joint PDF,

$$S_{\mathrm{bb}} = -k_B \Delta^2 \sum_i \sum_j P\left(\phi^i, \psi^j\right) \ln P\left(\phi^i, \psi^j\right), \tag{8}$$

which is identical to the two-DOF version of Eq. 5. For side chains, the number of DOFs (χ angles) varies between 1 and 5, where we used up to MIST3.

RESULTS AND DISCUSSION

Order parameter

To test whether the 500-ns simulation time was adequate for analyzing conformational motion, we calculated the backbone amide bond order parameters (see Supporting Materials and Methods for details). Based on the relaxation time of the angular reorientational correlation function $C_I(t)$ (Eq. 2; Figs. S1 and S2), we decided to use the 100–500-ns interval for all analysis. Our computational and experimental order parameters agreed reasonably well for nSH3 (Fig. S3). Upon complex formation, PRMs undergo larger changes in order parameter and RMSF of the backbone C$_\alpha$ atoms (Figs. S3–S6). This reflects that nSH3 remains stably folded, whereas PRMs undergo disorder-order transition as they bind. Similar behaviors were observed in conformational entropy changes, as discussed below.

Entropy change upon ligand binding

We calculated the backbone and side-chain conformational entropies separately or together. For higher accuracy, we used up to MIST3 approximation. The MIST1 entropy (Eq. 3) is the sum of entropies calculated for individual DOFs. Correlations among DOFs make the actual entropy less than the MIST1 entropy (Eqs. 5 and 7). In systems studied here, the MIST1 entropy takes up the dominant portion, whereas MIST2 or MIST3 entropies are slightly reduced (Fig. 2). This indicates that correlations among DOFs are not strong. To examine whether using the 100–500 ns interval was adequate for entropy calculation, we calculated the MIST2 entropy for time intervals starting from 100 ns in 20-ns increments. Plateauing of calculated entropies suggests that the 400-ns duration was reasonable (Fig. S7).

Backbone entropy change of nSH3

Previous NMR-based estimates of backbone entropy changes associated with the PRM:SH3 complex formation were −7.0 ± 4.3 cal/(mol•K) (8) and −5 ± 2 cal/(mol•K) (17). Although direct comparison is difficult because these values are for different SH3:PRM systems, our calculated values (top row of Table 1) are similar in magnitude. Comparing between the two complexes in this study, the backbone entropy change of nSH3 is smaller for the PRM$^{\mathrm{cAbl}}$-bound form than the PRM$^{\mathrm{NS1}}$-bound form.

As previously reported, ligand binding decreases the backbone entropy of the SH3 domain (8,17). However, it is the smallest among the entropy changes listed in Table 1. This reflects that the stable nSH3 fold is little affected by the binding of a PRM, which was also seen in the analysis of the order parameter and the backbone C$_\alpha$ RMSF (Supporting Materials and Methods).

Backbone entropy change of PRMs

PRMs undergo disorder-order transition upon binding to nSH3 so that their backbone conformational entropy

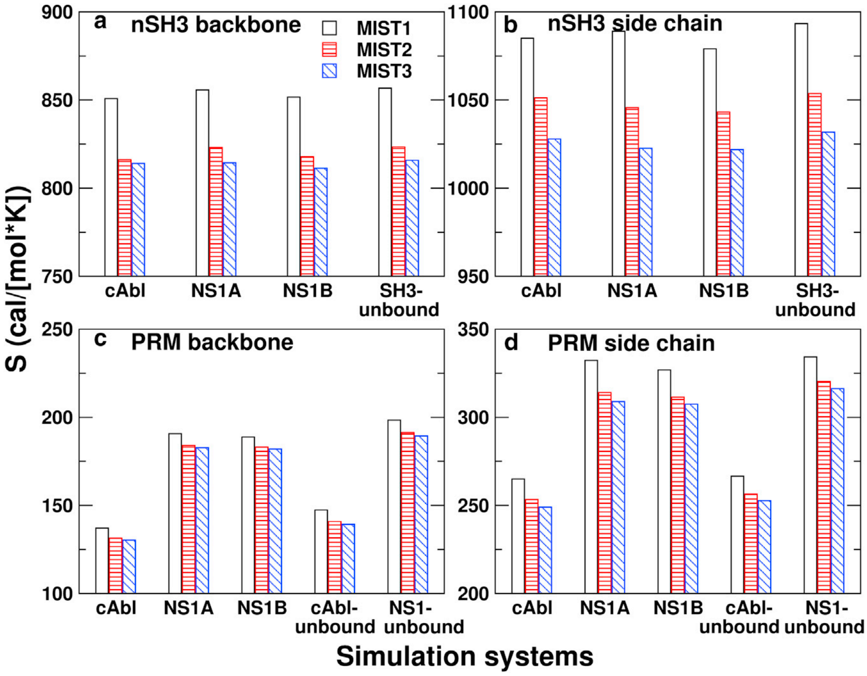

FIGURE 2 Comparison of MIST entropies. (*a* and *b*) nSH3 and (*c* and *d*) PRM are shown. Respective MIST calculations were performed separately for (*a* and *c*) the backbone and (*b* and *d*) side chains. Vertical axes in all panels are in the same range, 150 cal/(mol•K), to highlight relative differences. SDs in calculated entropies are at most 0.15 cal/(mol•K). To see this figure in color, go online.

changes are larger compared to nSH3 (Table 1, first versus second rows). Between the two ligands, although PRM^{cAbl} is shorter than PRM^{NS1}, it involves a greater backbone entropy loss (Table 1, second row). At the level of individual residues, PRM^{cAbl} shows large backbone entropy loss in the PxxP motif, especially A762, and also in the last two residues at the C-terminus (Fig. 3 *a*). The corresponding residue in PRM^{NS1} is P213 (Fig. 1), whose backbone is less flexible. The PxxP motif of PRM^{NS1} is surrounded by additional prolines, which impose a stronger conformational restraint on the backbone. This contributes to the small backbone entropy change upon binding. Furthermore, the two C-terminal residues of PRM^{NS1} show little changes in the backbone entropy upon binding (Fig. 3 *b*), suggesting that they remain mobile. The first two N-terminal residues in both PRMs also remain mobile.

Side-chain entropy change in nSH3

For nSH3, side-chain entropy changes are 2.1–3.8 times greater than backbone entropy changes (first versus third rows in Table 1). This is due to the restriction of the side-chain motion upon the binding of a PRM. However, residue-level analysis revealed that certain side chains gain entropy upon binding (Fig. 4). Side-chain entropies of R138, K155, and R162 in nSH3 increased substantially when complexed with PRM^{cAbl} and to a lesser extent with PRM^{NS1} (Fig. 4, *a* and *b*). Y190 at the C-terminus of nSH3 is located next to R138, and its side-chain entropy increased in both of the two SH3:PRM^{NS1} systems (Fig. 4, *b* and *c*). These residues are bulky and surface exposed, and none of them interacts directly with PRMs. Only K155 formed contact with the N-terminal tyrosine of the two PRMs (Fig. 1 *a*) but with less than 1% occupancy. Increase in the side-chain entropy of these residues should thus be an indirect effect of PRM binding. Supporting this idea is a previous study reporting strain propagation across the entire c-Src SH3 domain as a compensatory response to ligand binding (64). A detailed analysis of the intra-nSH3 contacts revealed that the side-chain entropy increase in remote residues is mostly a result of the propagation of changes in lateral contacts of surface residues upon ligand binding (see Fig. S9 and Tables S1–S3 for details). The breakage of hydrogen bonds plays a significant role in increasing the side-chain entropy, although rearrangements of lateral nonpolar contacts are also involved. This explains why side-chain entropy increase occurs for large charged or polar residues on the surface of the protein. An additional possibility is the perturbation of the surface hydration structure upon

TABLE 1 Entropy Changes upon Complex Formation

		nSH3:PRM^{cAbl}	nSH3:PRM^{NS1A}	nSH3:PRM^{NS1B}
Backbone	nSH3	−1.80 ± 0.215	−2.38 ± 0.204	−4.47 ± 0.184
	PRM	−8.99 ± 0.041	−6.74 ± 0.057	−7.43 ± 0.088
Side chain	nSH3	−3.83 ± 0.187	−9.13 ± 0.171	−9.82 ± 0.202
	PRM	−3.75 ± 0.114	−7.44 ± 0.161	−8.83 ± 0.154
Net Change		−28.64 ± 0.336	−36.56 ± 0.310	−38.99 ± 0.317

Numbers are in units of cal/(mol•K). MIST3 was used. Because correlations among DOFs are more extensive in the complex, the net change in entropy (bottom row) is greater in magnitude than the sum of backbone and side-chain entropy changes. Dependence of the calculated entropy on the bin size Δ is in Fig. S8, which has little impact on relative magnitudes of different entropy terms.

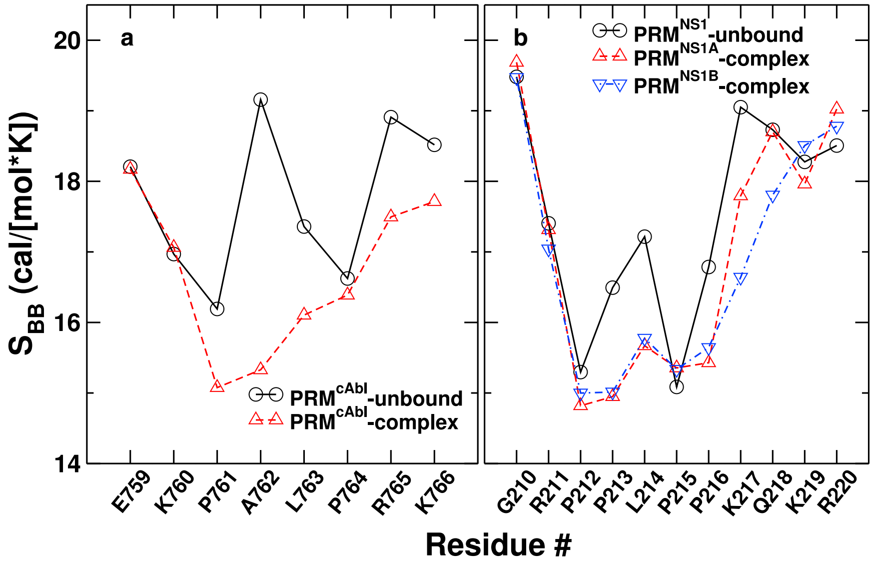

FIGURE 3 Per-residue backbone entropy of PRM in the complex and unbound states. (*a*) Shown is PRM^{cAbl}. (*b*) Shown is PRM^{NS1}. To see this figure in color, go online.

ligand binding that in turn can affect the mobility of surface-exposed side chains of nSH3 (65). Further studies are needed to elucidate the allosteric effect of ligand binding on the side-chain motion.

Residues that showed a substantial decrease in side-chain entropy are mainly in the ligand binding pocket. The largest side-chain entropy loss in nSH3 among all three systems was in two nonpolar residues, F141 and W169 (Fig. 4). Both are highly conserved across SH3 domains (46,66). They form high-occupancy nonpolar contacts with the PRM (Table 2), which restricts their side-chain motion. E149 in the RT loop and E166 in the n-Src loop that form hydrogen bonds with the C-terminal positively charged residues of PRM (Fig. 4 *d*) also lose side-chain entropy substantially (for simplicity, we call a salt bridge involving hydrogen atom also a hydrogen bond; Table 2). Other residues that form high-occupancy contacts with the PRM (Table 2) also contribute to the side-chain entropy loss but to a lesser extent.

Away from the binding interface, D174 in nSH3:PRM^{NS1A} and K178 in nSH3:PRM^{NS1B} in the distal loop also showed notable side-chain entropy loss (Fig. 4, *b–d*). This may be a long-range effect, similar to the entropy increase in distal residues upon ligand binding. A previous NMR study of ligand binding to c-Src SH3 domain showed that changes in motion occur both near and away from the ligand binding interface (17). Both D174 and K178 form hydrogen bonds with the nearby E176 in the distal loop with different contact occupancies. In isolated nSH3, their contact occupancies are 50.7% (D174-E176) and 78.7% (K178-E176). In nSH3:PRM^{cAbl}, these occupancies increase by less than 4.6% upon complex formation, which is consistent with their moderate side-chain entropy changes (Fig. 4 *a*). For nSH3:PRM^{NS1A}, the occupancy of D174-E176 increases to 90%, whereas for K178-E176, it decreases to 8.7% (cf., Table S2), which contributes to the relatively large decrease in side-chain entropy of D174 (Fig. 4 *b*). However, E176 did not experience any corresponding side-chain entropy loss. For nSH3:PRM^{NS1B}, the D174-E176 bond had nearly the same occupancy in the complex, 55.5%, and the occupancy of K178-E176 increased to 88.1%, again in line with the side-chain entropy loss of K178. Thus, the contact occupancy and side-chain entropy changes upon complex formation are somewhat correlated when the occupancy increases to a high value, which may be due to a restriction in side-chain motion. However, two residues forming a high-occupancy contact do not experience comparable side-chain entropy loss, as seen for E176.

Side-chain entropy change in PRMs

Similar to nSH3, residues in PRMs that showed large side-chain entropy loss (marked by *stars* in Fig. 5) formed high-occupancy contacts with nSH3 (Table 2), although the converse does not necessarily hold. Contact analysis suggests a different mechanism underlying the entropy changes between nSH3 and PRMs. For nSH3, the largest side-chain entropy losses were by residues that form nonpolar contacts (i.e., F141 and W169). But their binding partners in PRM do not experience correspondingly large entropy loss. For example, L763 in PRM^{cAbl} and L214 in PRM^{NS1} contact W169, but their side-chain entropy changes are not significant (Table 2). When a PRM binds, F141 and W169 of nSH3 become buried in the interface (Fig. 4 *c*), whereas their nonpolar contact residues in PRM are still partially exposed, which allows more room for motion. For PRM, on the other hand, all residues that had more than 2 cal/(mol•K) side-chain entropy loss formed high-occupancy hydrogen bonds with nSH3 (R767 in PRM^{cAbl}, R220 in PRM^{NS1A}, and K217 in PRM^{NS1B}; *single star* in Fig. 5 and Table 2). Compared to nonpolar contacts, hydrogen bonds are more directional, where the acceptor-hydrogen-donor angle is greater than

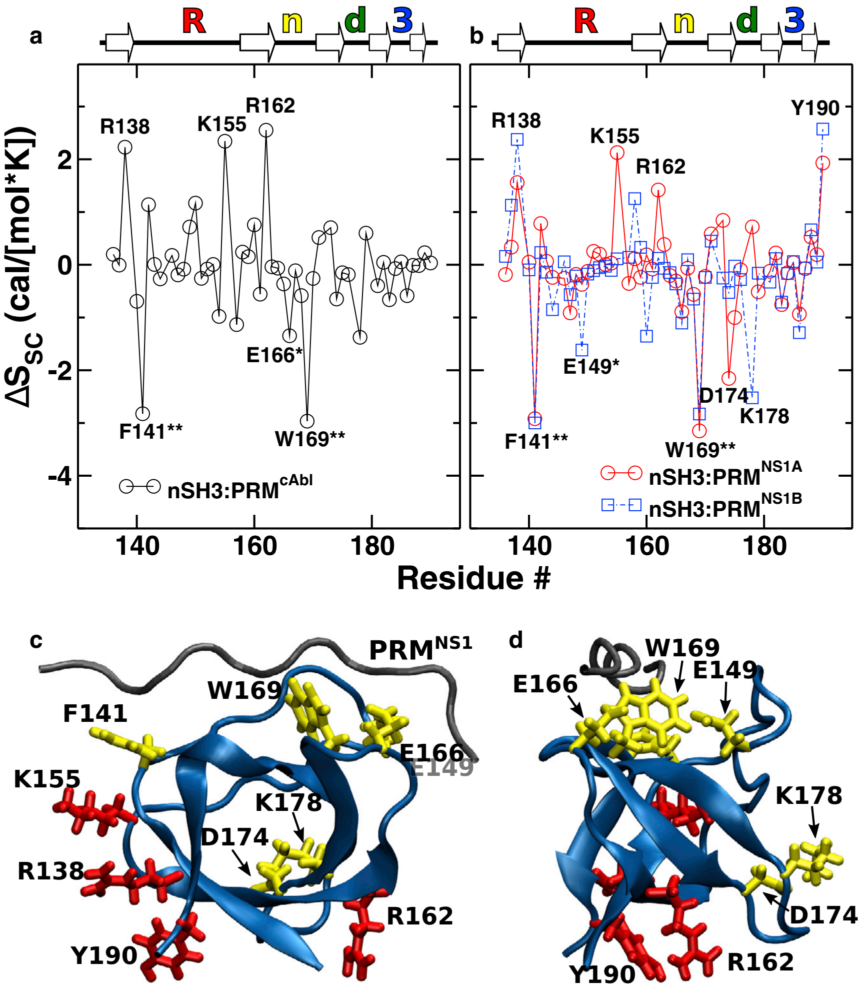

FIGURE 4 Per-residue side-chain entropy change of nSH3 upon ligand binding. Positive value means higher entropy in the complexed state. (*a*) nSH3:PRM^{cAbl} and (*b*) nSH3:PRM^{NS1} are shown. Major subdomains (Fig. 1) are marked above each panel: RT loop ("R"), n-Src loop ("n"), distal loop ("d"), and 3_{10} helix ("3"). (*c* and *d*) Locations of residues in nSH3 are marked in (*a*) and (*b*). Red/yellow: per-residue side-chain entropy increased/decreased is shown. (*c*) Side view: image shown viewed from below in Fig. 1 *b*. (*d*) View from the right of (*c*) is shown. To see this figure in color, go online.

120° (67,68). The directional constraint can suppress side-chain motion more effectively than nonpolar contacts do.

Net entropy change

When entropy change upon ligand binding is calculated for the whole system, the correlation effect between nSH3 and PRM additionally lower the entropy of the complex relative to the unbound states. This causes the net entropy change of the whole system to be greater than the sum of individual entropy changes (Table 1, last versus other rows). Between nSH3:PRM^{cAbl} and nSH3:PRM^{NS1}, the latter involves a greater change in side-chain entropy. Although this is partly due to PRM^{NS1} being longer than PRM^{cAbl}, the former also involves a larger per-residue entropy loss (Fig. 5).

The net entropy change in ligand binding in nSH3:PRM^{NS1} is 7.9–10.4 cal/(mol•K) greater than that of nSH3:PRM^{cAbl} (Table 1, last row). At 300 K, this corresponds to 2.4–3.1 kcal/mol, which is comparable to the free energy of a hydrogen bond (69). With nSH3:PRM^{NS1} also forming more contacts (Table 2), the emerging picture is that PRM^{NS1} achieves a higher binding affinity to nSH3, in which the favorable enthalpy change afforded by the extensive contact formation is greater than the entropy loss, which is consistent with its role as a viral peptide (43). The weaker binding and relatively smaller changes of entropy in PRM^{cAbl} is also consistent with the experiment (40), and it enables easier regulation of the interaction with nSH3 of CrkII.

It is notable that the side-chain dynamics is different from the backbone dynamics. The backbone entropy loss of PRM^{cAbl} is larger than that of PRM^{NS1}, whereas the converse holds for the side-chain entropy loss. If only the backbone order parameter or backbone entropy were considered, which has been easier to measure experimentally, one might conclude that PRM^{NS1} is more flexible than PRM^{cAbl} in the bound state. It is thus essential to also consider the side-chain dynamics to establish a more complete understanding of the entropy contribution.

CONCLUSIONS

Dissecting the relative contributions of backbone and side-chain entropies, for individual residues or together, provides

TABLE 2 List of High-Occupancy Contacts and Side-Chain Entropy Changes

	H-Bond			Nonpolar Contact		
	nSH3	PRM	Occupancy	nSH3	PRM	Occupancy
nSH3:PRM^{cAbl}	E166^{n} (−1.35)	R767 (−3.48)	0.987	F141^{R} (−2.82)	K760 (−0.45)	0.930
	Y1863 (−0.59)	P761 (+0.02)	0.939	F141^{R} (−2.82)	P761 (+0.02)	0.769
	–	–	–	F143^{R} (+0.00)	L763 (−0.63)	0.928
	–	–	–	Q168^{n} (−0.58)	P764 (+0.24)	0.949
	–	–	–	W169^{n} (−2.97)	L763 (−0.63)	0.840
	–	–	–	P183^{3} (−0.66)	L763 (−0.63)	0.876
	–	–	–	P185^{3} (+0.05)	P764 (+0.24)	0.772
	–	–	–	Y186^{3} (−0.59)	P761 (+0.02)	0.876
nSH3:PRM^{NS1A}	D142^{R} (+0.78)	R211 (−1.26)	0.839	F141^{R} (−2.92)	R211 (−1.26)	0.900
	D147^{R} (−0.91)	K217 (−1.41)	0.839	F141^{R} (−2.92)	P212 (−0.03)	0.785
	D150^{R} (−0.12)	K217 (−1.41)	0.943	F143^{R} (+0.06)	L214 (−0.84)	0.955
	E166^{n} (−0.89)	R220 (−4.50)	0.968	Q168^{n} (−0.56)	P215 (+0.93)	0.970
	Y186^{3} (−0.94)	P212 (−0.03)	0.978	W169^{n} (−3.15)	L214 (−0.84)	0.897
	–	–	–	W169^{n} (−3.15)	K217 (−1.41)	0.951
	–	–	–	P183^{3} (−0.75)	L214 (−0.84)	0.886
	–	–	–	P185^{3} (+0.04)	P215 (+0.93)	0.870
	–	–	–	Y186^{3} (−0.94)	R211 (−1.26)	0.831
	–	–	–	Y186^{3} (−0.94)	P212 (−0.03)	0.926
	–	–	–	Y186^{3} (−0.94)	L214 (−0.84)	0.754
nSH3:PRM^{NS1B}	D142^{R} (+0.23)	R211 (−2.11)	0.721	F141^{R} (−3.00)	R211 (−2.11)	0.928
	D147^{R} (−1.57)	K217 (−4.47)	0.933	F141^{R} (−3.00)	P212 (+0.08)	0.746
	E149^{R} (−0.37)	K217 (−4.47)	0.825	F143^{R} (−0.14)	L214 (−1.00)	0.949
	E149^{R} (−0.37)	R220 (−1.71)	0.799	Q168^{n} (−0.65)	P215 (+0.94)	0.939
	D150^{R} (−0.18)	K217 (−4.47)	0.985	W169^{n} (−2.83)	L214 (−1.00)	0.872
	E166^{n} (−1.10)	R220 (−1.71)	0.783	W169^{n} (−2.83)	K217 (−4.47)	0.920
	Y186^{3} (−1.29)	P212 (+0.08)	0.979	P183^{3} (−0.71)	L214 (−1.00)	0.914
	–	–	–	P185^{3} (+0.06)	P215 (+0.94)	0.826
	–	–	–	Y186^{3} (−1.29)	R211 (−2.11)	0.858
	–	–	–	Y186^{3} (−1.29)	P212 (+0.08)	0.926
	–	–	–	Y186^{3} (−1.29)	L214 (−1.00)	0.741

Hydrogen bond (H-Bond) includes salt bridges. Residues of nSH3 are marked with superscripts with the corresponding subdomains (^{3}: 3_{10} helix; ^{R}: RT loop; and ^{n}: n-Src loop). Side-chain entropy change of each residue upon complex formation (in cal/(mol•K)) is in parentheses.

important details about the binding of PRMs to nSH3. Present results suggest that side chains play a critical role for determining entropy changes associated with the binding. For the stably folded nSH3, side-chain entropy change is larger than that of the backbone. For PRMs, as they belong to IDRs, both the backbone and side chains contribute comparably to the entropy change. As a result, considerable fraction of the net entropy change is due to PRMs, even though they are much smaller than nSH3 in size. We also note that, because entropy is a state function, only separate simulations of the uncomplexed PRMs and nSH3 and nSH3:PRM complexes were needed for calculation. Although analysis of the binding and unbinding processes of the PRM will provide additional kinetic information, it is beyond the scope of this study.

We found that ligand binding induces per-residue side-chain entropy changes both at the nSH3:PRM interface and across nSH3. For residues of nSH3 that form high-occupancy contacts with PRM, side-chain entropy decreases to varying extents, the largest of which were the highly conserved and nonpolar F141 and W169. Analogously, for an SH2 domain, ligand binding did not incur any significant changes in the backbone motion, whereas a few "hotspot" residues at the interface made a large contribution to the binding free energy (70). Unlike nSH3, the side-chain entropy loss of PRMs is large for residues that form high-occupancy hydrogen bonds. Consistent with the nonreciprocal changes in side-chain entropy at the interface, a previous NMR study of a calmodulin domain and its target domains noted a "surprisingly noncomplementary" distribution of motion at the interface (71). Side-chain entropy changes in remote surface-exposed residues likely arises from propagation of the rearrangements in the contacts across surface residues upon ligand binding. A long-range effect of ligand binding has also been observed in other systems including SH3 domains (17,64) and an MDM2 domain with p53-derived peptides (72). Entropy changes in charged or polar residues in distal regions may play an allosteric role for electrostatic interactions with other domains (73,74).

Between nSH3:PRM^{cAbl} and nSH3:PRM^{NS1}, the higher binding affinity of the latter (40,43) appears to be driven by the favorable enthalpy change that compensates for the unfavorable entropy loss. The smaller backbone entropy change in PRM^{NS1} is due to its central region that remains relatively rigid in the unbound state and also due to its C-terminal region that form "fuzzy" contacts so that the region stays flexible in the bound state, whereas its side chains

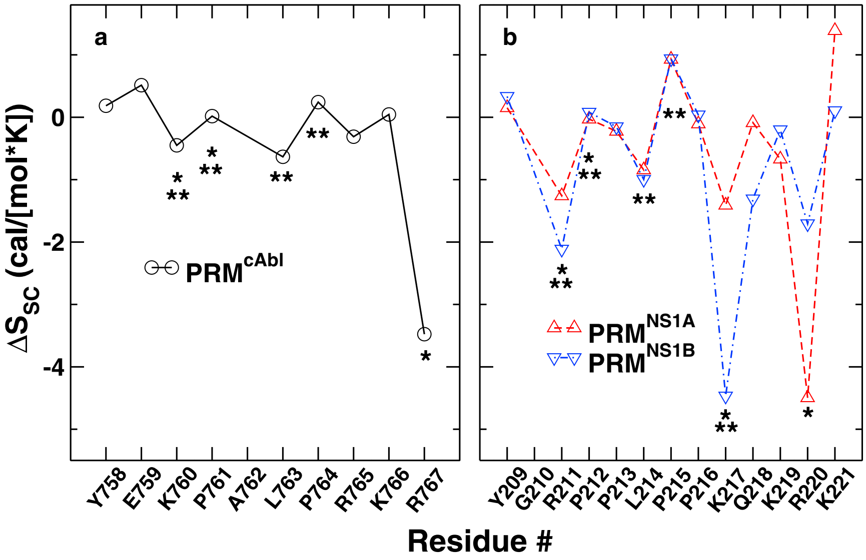

FIGURE 5 Per-residue side-chain entropy change of PRMs upon binding to nSH3. (*a*) nSH3:PRM^{cAbl} and (*b*) nSH3:PRM^{NS1} are shown. Residues that form high-occupancy contacts with nSH3 (Table 2) are marked by stars. Hydrogen bond: one star. Nonpolar: two stars. To see this figure in color, go online.

lose entropy substantially. Taken together, these results elucidate the role of entropy hotspots in influencing the conformational flexibility of the complex.

Decomposition of the free energy contributions of hotspot residues (75) into enthalpic and entropic contributions may provide new insight into how specificity is tuned for proteins with multiple binding partners (71). Moreover, the sites that are distant from the binding interface but undergo considerable changes in conformational entropy may conversely regulate protein-protein interactions, called dynamic allostery (76,77). In this regard, the allosteric hotspots may serve as viable targets for the rational development of protein-protein interaction modulators.

This work combining entropy and contact analysis, together with experimental studies using various NMR relaxation methods (78,79), will facilitate the understanding of the side-chain dynamics and its role in molecular recognition. Furthermore, interfacial water molecules likely play a significant role as well (16,65,80,81), which is a subject of future studies.

SUPPORTING MATERIAL

Supporting Material can be found online at https://doi.org/10.1016/j.bpj.2020.03.026.

AUTHOR CONTRIBUTIONS

J.S. designed research, performed and analyzed simulation, and wrote the manuscript. Q.S. processed experimental data. J.-H.C. designed research, performed and analyzed experiment, and wrote the manuscript. W.H. designed research, analyzed simulation, and wrote the manuscript.

ACKNOWLEDGMENTS

Simulations were performed on machines at the Texas A&M High-Performance Research Computing Facility.

Research reported in this publication was supported by the National Institute of General Medical Sciences of the U.S. National Institutes of Health under award number R01GM127723.

SUPPORTING CITATIONS

References (82,83) appear in the Supporting Material.

REFERENCES

1. Uversky, V. N., and A. K. Dunker. 2008. Biochemistry. Controlled chaos. *Science*. 322:1340–1341.
2. Dunker, A. K., C. J. Brown, …, Z. Obradović. 2002. Intrinsic disorder and protein function. *Biochemistry*. 41:6573–6582.
3. Tompa, P., and M. Fuxreiter. 2008. Fuzzy complexes: polymorphism and structural disorder in protein-protein interactions. *Trends Biochem. Sci.* 33:2–8.
4. Mittag, T., L. E. Kay, and J. D. Forman-Kay. 2010. Protein dynamics and conformational disorder in molecular recognition. *J. Mol. Recognit.* 23:105–116.
5. Uversky, V. N. 2013. A decade and a half of protein intrinsic disorder: biology still waits for physics. *Protein Sci.* 22:693–724.
6. Wright, P. E., and H. J. Dyson. 2015. Intrinsically disordered proteins in cellular signalling and regulation. *Nat. Rev. Mol. Cell Biol.* 16:18–29.
7. Shammas, S. L., M. D. Crabtree, …, J. Clarke. 2016. Insights into coupled folding and binding mechanisms from kinetic studies. *J. Biol. Chem.* 291:6689–6695.
8. Zeng, D., Q. Shen, and J. H. Cho. 2017. Thermodynamic contribution of backbone conformational entropy in the binding between SH3 domain and proline-rich motif. *Biochem. Biophys. Res. Commun.* 484:21–26.
9. Dyson, H. J., and P. E. Wright. 2005. Intrinsically unstructured proteins and their functions. *Nat. Rev. Mol. Cell Biol.* 6:197–208.
10. Kay, B. K., M. P. Williamson, and M. Sudol. 2000. The importance of being proline: the interaction of proline-rich motifs in signaling proteins with their cognate domains. *FASEB J.* 14:231–241.
11. Macias, M. J., S. Wiesner, and M. Sudol. 2002. WW and SH3 domains, two different scaffolds to recognize proline-rich ligands. *FEBS Lett.* 513:30–37.

12. Theillet, F. X., L. Kalmar, …, V. N. Uversky. 2013. The alphabet of intrinsic disorder: I. Act like a Pro: on the abundance and roles of proline residues in intrinsically disordered proteins. *Intrinsically Disord. Proteins.* 1:e24360.

13. Rath, A., A. R. Davidson, and C. M. Deber. 2005. The structure of "unstructured" regions in peptides and proteins: role of the polyproline II helix in protein folding and recognition. *Biopolymers.* 80:179–185.

14. Mayer, B. J. 2001. SH3 domains: complexity in moderation. *J. Cell Sci.* 114:1253–1263.

15. Li, S. S. 2005. Specificity and versatility of SH3 and other proline-recognition domains: structural basis and implications for cellular signal transduction. *Biochem. J.* 390:641–653.

16. Palencia, A., E. S. Cobos, …, I. Luque. 2004. Thermodynamic dissection of the binding energetics of proline-rich peptides to the Abl-SH3 domain: implications for rational ligand design. *J. Mol. Biol.* 336:527–537.

17. Wang, C., N. H. Pawley, and L. K. Nicholson. 2001. The role of backbone motions in ligand binding to the c-Src SH3 domain. *J. Mol. Biol.* 313:873–887.

18. Creamer, T. P. 1998. Left-handed polyproline II helix formation is (very) locally driven. *Proteins.* 33:218–226.

19. Ferreon, J. C., and V. J. Hilser. 2004. Thermodynamics of binding to SH3 domains: the energetic impact of polyproline II (PII) helix formation. *Biochemistry.* 43:7787–7797.

20. Kasinath, V., K. A. Sharp, and A. J. Wand. 2013. Microscopic insights into the NMR relaxation-based protein conformational entropy meter. *J. Am. Chem. Soc.* 135:15092–15100.

21. Baxa, M. C., E. J. Haddadian, …, T. R. Sosnick. 2014. Loss of conformational entropy in protein folding calculated using realistic ensembles and its implications for NMR-based calculations. *Proc. Natl. Acad. Sci. USA.* 111:15396–15401.

22. Sharp, K. A., E. O'Brien, …, A. J. Wand. 2015. On the relationship between NMR-derived amide order parameters and protein backbone entropy changes. *Proteins.* 83:922–930.

23. Caro, J. A., K. W. Harpole, …, A. J. Wand. 2017. Entropy in molecular recognition by proteins. *Proc. Natl. Acad. Sci. USA.* 114:6563–6568.

24. Wand, A. J., and K. A. Sharp. 2018. Measuring entropy in molecular recognition by proteins. *Annu. Rev. Biophys.* 47:41–61.

25. Karplus, M., and J. N. Kushick. 1981. Method for estimating the configurational entropy of macromolecules. *Macromolecules.* 14:325–332.

26. Karplus, M., T. Ichiye, and B. M. Pettitt. 1987. Configurational entropy of native proteins. *Biophys. J.* 52:1083–1085.

27. Grünberg, R., M. Nilges, and J. Leckner. 2006. Flexibility and conformational entropy in protein-protein binding. *Structure.* 14:683–693.

28. Lee, K. H., D. Xie, …, L. M. Amzel. 1994. Estimation of changes in side chain configurational entropy in binding and folding: general methods and application to helix formation. *Proteins.* 20:68–84.

29. Doig, A. J., and M. J. Sternberg. 1995. Side-chain conformational entropy in protein folding. *Protein Sci.* 4:2247–2251.

30. Wang, W., W. A. Lim, …, P. A. Kollman. 2001. An analysis of the interactions between the Sem-5 SH3 domain and its ligands using molecular dynamics, free energy calculations, and sequence analysis. *J. Am. Chem. Soc.* 123:3986–3994.

31. Hou, T., K. Chen, …, W. Wang. 2006. Computational analysis and prediction of the binding motif and protein interacting partners of the Abl SH3 domain. *PLoS Comput. Biol.* 2:e1.

32. DuBay, K. H., and P. L. Geissler. 2009. Calculation of proteins' total side-chain torsional entropy and its influence on protein-ligand interactions. *J. Mol. Biol.* 391:484–497.

33. King, B. M., and B. Tidor. 2009. MIST: maximum information spanning trees for dimension reduction of biological data sets. *Bioinformatics.* 25:1165–1172.

34. King, B. M., N. W. Silver, and B. Tidor. 2012. Efficient calculation of molecular configurational entropies using an information theoretic approximation. *J. Phys. Chem. B.* 116:2891–2904.

35. Feller, S. M. 2001. Crk family adaptors-signalling complex formation and biological roles. *Oncogene.* 20:6348–6371.

36. Rodrigues, S. P., K. E. Fathers, …, M. Park. 2005. CrkI and CrkII function as key signaling integrators for migration and invasion of cancer cells. *Mol. Cancer Res.* 3:183–194.

37. Wu, X., B. Knudsen, …, J. Kuriyan. 1995. Structural basis for the specific interaction of lysine-containing proline-rich peptides with the N-terminal SH3 domain of c-Crk. *Structure.* 3:215–226.

38. Matsuda, M., S. Ota, …, T. Kurata. 1996. Interaction between the amino-terminal SH3 domain of CRK and its natural target proteins. *J. Biol. Chem.* 271:14468–14472.

39. Takino, T., M. Tamura, …, K. M. Yamada. 2003. Tyrosine phosphorylation of the CrkII adaptor protein modulates cell migration. *J. Cell Sci.* 116:3145–3155.

40. Bhatt, V. S., D. Zeng, …, J. H. Cho. 2016. Binding mechanism of the N-terminal SH3 domain of CrkII and proline-rich motifs in cAbl. *Biophys. J.* 110:2630–2641.

41. Horimoto, T., and Y. Kawaoka. 2005. Influenza: lessons from past pandemics, warnings from current incidents. *Nat. Rev. Microbiol.* 3:591–600.

42. Melén, K., L. Kinnunen, …, I. Julkunen. 2007. Nuclear and nucleolar targeting of influenza A virus NS1 protein: striking differences between different virus subtypes. *J. Virol.* 81:5995–6006.

43. Shen, Q., D. Zeng, …, J. H. Cho. 2017. The molecular mechanisms underlying the hijack of host proteins by the 1918 Spanish influenza virus. *ACS Chem. Biol.* 12:1199–1203.

44. Shen, Q., J. Shi, …, J. H. Cho. 2018. Molecular mechanisms of tight binding through fuzzy interactions. *Biophys. J.* 114:1313–1320.

45. Kleinpeter, A. B., A. S. Jureka, …, C. M. Petit. 2018. Structural analyses reveal the mechanism of inhibition of influenza virus NS1 by two antiviral compounds. *J. Biol. Chem.* 293:14659–14668.

46. Larson, S. M., A. A. Di Nardo, and A. R. Davidson. 2000. Analysis of covariation in an SH3 domain sequence alignment: applications in tertiary contact prediction and the design of compensating hydrophobic core substitutions. *J. Mol. Biol.* 303:433–446.

47. Brooks, B. R., R. E. Bruccoleri, …, M. Karplus. 1983. CHARMM: a program for macromolecular energy, minimization, and dynamics calculations. *J. Comput. Chem.* 4:187–217.

48. Brooks, B. R., C. L. Brooks, III, …, M. Karplus. 2009. CHARMM: the biomolecular simulation program. *J. Comput. Chem.* 30:1545–1614.

49. Hart, K., N. Foloppe, …, A. D. Mackerell, Jr. 2012. Optimization of the CHARMM additive force field for DNA: improved treatment of the BI/BII conformational equilibrium. *J. Chem. Theory Comput.* 8:348–362.

50. Jorgensen, W., J. Chandrasekhar, …, M. L. Klein. 1983. Comparison of simple potential functions for simulating liquid water. *J. Chem. Phys.* 79:926–935.

51. Ryckaert, J.-P., G. Ciccotti, and H. J. Berendsen. 1977. Numerical integration of the cartesian equations of motion of a system with constraints: molecular dynamics of n-alkanes. *J. Comput. Phys.* 23:327–341.

52. Feller, S. E., R. W. Pastor, …, B. R. Brooks. 1996. Effect of electrostatic force truncation on interfacial and transport properties of water. *J. Phys. Chem.* 100:17011–17020.

53. Hynninen, A. P., and M. F. Crowley. 2014. New faster CHARMM molecular dynamics engine. *J. Comput. Chem.* 35:406–413.

54. Humphrey, W., A. Dalke, and K. Schulten. 1996. VMD: visual molecular dynamics. *J. Mol. Graph.* 14:33–38, 27–28..

55. Pettersen, E. F., T. D. Goddard, …, T. E. Ferrin. 2004. UCSF Chimera–a visualization system for exploratory research and analysis. *J. Comput. Chem.* 25:1605–1612.

56. Lipari, G., and A. Szabo. 1982. Model-free approach to the interpretation of nuclear magnetic resonance relaxation in macromolecules. 1. Theory and range of validity. *J. Am. Chem. Soc.* 104:4546–4559.
57. Chandrasekhar, I., G. M. Clore, …, B. R. Brooks. 1992. A 500 ps molecular dynamics simulation study of interleukin-1 beta in water. Correlation with nuclear magnetic resonance spectroscopy and crystallography. *J. Mol. Biol.* 226:239–250.
58. Trbovic, N., J. H. Cho, …, A. G. Palmer, III. 2009. Protein side-chain dynamics and residual conformational entropy. *J. Am. Chem. Soc.* 131:615–622.
59. Mandel, A. M., M. Akke, and A. G. Palmer, III. 1995. Backbone dynamics of *Escherichia coli* ribonuclease HI: correlations with structure and function in an active enzyme. *J. Mol. Biol.* 246:144–163.
60. Cole, R., and J. P. Loria. 2003. FAST-Modelfree: a program for rapid automated analysis of solution NMR spin-relaxation data. *J. Biomol. NMR.* 26:203–213.
61. Lipari, G., and A. Szabo. 1982. Model-free approach to the interpretation of nuclear magnetic resonance relaxation in macromolecules. 2. Analysis of experimental results. *J. Am. Chem. Soc.* 104:4559–4570.
62. Stites, W. E., and J. Pranata. 1995. Empirical evaluation of the influence of side chains on the conformational entropy of the polypeptide backbone. *Proteins.* 22:132–140.
63. IUPAC-IUB Commission on Biochemical Nomenclature (CBN). 1970. Abbreviations and symbols for the description of the conformation of polypeptide chains. *J. Biol. Chem.* 245:6489–6497.
64. Cordier, F., C. Wang, …, L. K. Nicholson. 2000. Ligand-induced strain in hydrogen bonds of the c-Src SH3 domain detected by NMR. *J. Mol. Biol.* 304:497–505.
65. Zafra-Ruano, A., and I. Luque. 2012. Interfacial water molecules in SH3 interactions: getting the full picture on polyproline recognition by protein-protein interaction domains. *FEBS Lett.* 586:2619–2630.
66. Harkiolaki, M., M. Lewitzky, …, S. M. Feller. 2003. Structural basis for SH3 domain-mediated high-affinity binding between Mona/Gads and SLP-76. *EMBO J.* 22:2571–2582.
67. De Loof, H., L. Nilsson, and R. Rigler. 1992. Molecular dynamics simulation of galanin in aqueous and nonaqueous solution. *J. Am. Chem. Soc.* 114:4028–4035.
68. Wood, P. A., F. H. Allen, and E. Pidcock. 2009. Hydrogen-bond directionality at the donor H atom – analysis of interaction energies and database statistics. *CrystEngComm.* 11:1563–1571.
69. Fersht, A. R. 1987. The hydrogen bond in molecular recognition. *Trends Biochem. Sci.* 12:301–304.
70. Ward, J. M., N. M. Gorenstein, …, C. B. Post. 2010. Constraining binding hot spots: NMR and molecular dynamics simulations provide a structural explanation for enthalpy-entropy compensation in SH2-ligand binding. *J. Am. Chem. Soc.* 132:11058–11070.
71. Marlow, M. S., J. Dogan, …, A. J. Wand. 2010. The role of conformational entropy in molecular recognition by calmodulin. *Nat. Chem. Biol.* 6:352–358.
72. Schon, O., A. Friedler, …, A. R. Fersht. 2004. Binding of p53-derived ligands to MDM2 induces a variety of long range conformational changes. *J. Mol. Biol.* 336:197–202.
73. Ozkirimli, E., S. S. Yadav, …, C. B. Post. 2008. An electrostatic network and long-range regulation of Src kinases. *Protein Sci.* 17:1871–1880.
74. DuBay, K. H., G. R. Bowman, and P. L. Geissler. 2015. Fluctuations within folded proteins: implications for thermodynamic and allosteric regulation. *Acc. Chem. Res.* 48:1098–1105.
75. Clackson, T., and J. A. Wells. 1995. A hot spot of binding energy in a hormone-receptor interface. *Science.* 267:383–386.
76. Tzeng, S. R., and C. G. Kalodimos. 2012. Protein activity regulation by conformational entropy. *Nature.* 488:236–240.
77. Motlagh, H. N., J. O. Wrabl, …, V. J. Hilser. 2014. The ensemble nature of allostery. *Nature.* 508:331–339.
78. Stafford, K. A., F. Ferrage, …, A. G. Palmer, III. 2013. Side chain dynamics of carboxyl and carbonyl groups in the catalytic function of *Escherichia coli* ribonuclease H. *J. Am. Chem. Soc.* 135:18024–18027.
79. Weininger, U. 2019. Optimal isotope labeling of aromatic amino acid side chains for NMR studies of protein dynamics. *Methods Enzymol.* 614:67–86.
80. Palencia, A., A. Camara-Artigas, …, I. Luque. 2010. Role of interfacial water molecules in proline-rich ligand recognition by the Src homology 3 domain of Abl. *J. Biol. Chem.* 285:2823–2833.
81. Martin-Garcia, J. M., J. Ruiz-Sanz, and I. Luque. 2012. Interfacial water molecules in SH3 interactions: a revised paradigm for polyproline recognition. *Biochem. J.* 442:443–451.
82. Jarymowycz, V. A., and M. J. Stone. 2006. Fast time scale dynamics of protein backbones: NMR relaxation methods, applications, and functional consequences. *Chem. Rev.* 106:1624–1671.
83. Maragakis, P., K. Lindorff-Larsen, …, D. E. Shaw. 2008. Microsecond molecular dynamics simulation shows effect of slow loop dynamics on backbone amide order parameters of proteins. *J. Phys. Chem. B.* 112:6155–6158.

Biophysical Journal, Volume *118*

Supplemental Information

Entropy Hotspots for the Binding of Intrinsically Disordered Ligands to a Receptor Domain

Jie Shi, Qingliang Shen, Jae-Hyun Cho, and Wonmuk Hwang

Analysis of order parameters and backbone fluctuations

The order parameter ranges between 0 (flexible) and 1 (rigid) (1, 2). To ensure convergence of calculated values, we calculated the angular reorientational correlation function $C_I(t)$(3) (Eq. 2; Fig. S1). The resulting relaxation time is generally longer in flexible regions, the longest being 46.6 ns, for K189 of nSH3 in the nSH3:PRM$^{\mathrm{NS1B}}$ complex (Fig. S2a). To minimize any potential influence of the initially prepared state, we excluded the first 100 ns from our analysis.

For both nSH3:PRM$^{\mathrm{cAbl}}$ and nSH3:PRM$^{\mathrm{NS1}}$, the calculated and experimentally measured S^2 for the nSH3 domain overall agree (Fig. S3). Regions with low S^2 are in flexible loops and terminal ends that also show high root-mean-square fluctuation (RMSF) of C$_\alpha$ atoms, though the correlation between S^2 and C$_\alpha$ RMSF is weak (Fig. S3 *vs.* S4). The standard deviation in calculated S^2 is generally larger for flexible regions (lower S^2), but overall it is much smaller than S^2 itself (Fig. S3c,d). For most residues in nSH3, both S^2 and C$_\alpha$ RMSF do not change significantly upon ligand binding, which suggests that there is no major change in the flexibility of the backbone (4). Except for terminal residues, the C$_\alpha$ RMSF is less than 1 Å, which also shows that nSH3 is stably folded and does not undergo any major conformational change when a PRM binds (Fig. S4).

nSH3:PRM$^{\mathrm{NS1A}}$ and nSH3:PRM$^{\mathrm{NS1B}}$ are two different structures of the same complex. Our previous 100-ns MD simulation did not find convergence in their conformational behaviors (5). With a 500-ns simulation time in the present study, S^2 as well as RMSF of nSH3 in the two structures follow similar profiles (Fig. S3b and Fig. S4b).

In contrast to nSH3, S^2 for PRM increases significantly upon binding (Fig. S5) (4). The largest increase was around the PxxP motif (P761–P764 in PRM$^{\mathrm{cAbl}}$ and P212–P215 in PRM$^{\mathrm{NS1}}$) that forms hydrophobic contacts with nSH3 (6). K217–R220 in PRM$^{\mathrm{NS1}}$ also showed a large increase in S^2 as they form electrostatic contacts with negatively charged residues in nSH3 (Fig. S5b) (5). Corresponding to K217 of PRM$^{\mathrm{NS1}}$ is K766 of PRM$^{\mathrm{cAbl}}$ (Fig. 1a), which did not change significantly in S^2 since it forms only low-occupancy contacts, the highest being 29% with W169 of nSH3 (Fig. S5a). Also note that, S^2 of PRMs in the complex is overall lower than that of nSH3 (Fig S3 *vs.* S5), indicating that PRMs remain comparatively flexible in the complex. The C$_\alpha$ RMSF of PRMs is mostly over 2 Å when unbound, and the value decreases for all residues upon binding to nSH3, which is another indicator of their conformational changes (Fig. S6).

Allosteric increase in side-chain entropy

To elucidate how ligand binding leads to increase in the side-chain entropy of certain residues distal to the ligand-binding interface, we examined differences in intra-nSH3 contacts between the liganded and unliganded states. In Fig. 4, two distal residues, D174 and K178 lose side-chain entropy in nSH3:PRM$^{\mathrm{NS1A}}$ and nSH3:PRM$^{\mathrm{NS1B}}$, which are explained in the main text in terms of changes in contacts with other residues. Here we consider residues that experience increase in side-chain entropy.

We focused on intra-nSH3 contacts with occupancy greater than 50% in either unliganded or liganded states, and the difference in occupancy between the two states larger than 10%. Among the selected contacts, we found that hydrogen bond (H-bond) occupancy and side-chain entropy change oppositely, where increase (decrease) in H-bond occupancy corresponds to decrease (increase) in side-chain entropy. (Tables S1–S3). Though there is little quantitative correlation, this trend is more evident for residues with relatively large side-chain entropy changes ($|\Delta S_{\mathrm{SC}}| > 1$ cal/[mol·K]). For a given residue pair, side-chain entropy changes are not symmetric since the two residues may respectively form additional contacts with other residues.

In comparison to H-bonds, there were more intra-nSH3 nonpolar contacts (23 to 31) that met our selection criteria. However, we did not find any clear relation between the nonpolar contact occupancy and the side-chain entropy changes. When a nonpolar contact breaks, the residues may form different nonpolar contacts due to the hydrophobic effect. In contrast, polar or charged groups on the surface of the protein may associate with water molecules after breaking H-bonds, thereby increasing side-chain entropy. Indeed, all the distal residues that had large side-chain entropy changes were surface-exposed polar or charged residues (Fig. 4c,d). Yet, some of them may also involve nonpolar contacts via the nonpolar part of their side chains, as explained below.

Among the residues in Tables S1–S3, we focus on those away from the ligand-binding interface and also had large side-chain entropy increase: K155 and R162 in nSH3:PRM$^{\mathrm{cAbl}}$ (Table S1), K155 and Y190 in nSH3:PRM$^{\mathrm{NS1A}}$ (Table S2), and Y190 in nSH3:PRM$^{\mathrm{NS1B}}$ (Table S3). In an isolated nSH3, both the backbone and the side chain of K155 form stable H-bonds with the side chain of D142 (Fig. S9a). Upon ligand binding, PRM residues K760 in nSH3:PRM$^{\mathrm{cAbl}}$ and R211 in nSH3:PRM$^{\mathrm{NS1A}}$ form H-bonds with D142, which impedes its H-bond with K155 (Fig. S9b,c). In contrast, the D142–K155 H-bond in nSH3:PRM$^{\mathrm{NS1B}}$ is less perturbed as R211 of the PRM mostly forms a H-bond with the backbone carbonyl oxygen of nSH3 D142 (Fig. S9c). Thus, increase in the side-chain entropy of K155 in nSH3:PRM$^{\mathrm{cAbl}}$ and nSH3:PRM$^{\mathrm{NS1A}}$ is due to the loss of its H-bond with D142 upon ligand binding.

For the Y136–Y190 H-bond that had occupancy decrease in nSH3:PRM$^{\mathrm{NS1A}}$ and nSH3:PRM$^{\mathrm{NS1B}}$ (Tables S2 and S3), the residues are respectively at the N- and C-termini of nSH3 (Fig. S9f). Between the two, Y136 also formed high-occupancy nonpolar contacts with other residues, *i.e.*, R160 (100% occupancy in both nSH3:PRM$^{\mathrm{NS1A}}$ and nSH3:PRM$^{\mathrm{NS1B}}$) and I158 (90.7% in nSH3:PRM$^{\mathrm{NS1A}}$ and 93.6% in nSH3:PRM$^{\mathrm{NS1B}}$). In comparison, other contacts that Y190 formed were lower in occupancy. They were also nonpolar, with the highest occupancy being 72.3% (R138 in nSH3:PRM$^{\mathrm{NS1A}}$; the contact broke at 413 ns and did not form again) and 52.9% (V137 in nSH3:PRM$^{\mathrm{NS1B}}$). This suggests that, when the Y136–Y190 H-bond breaks, Y190 experiences a greater increase in side-chain entropy.

For R162, the increase in its side-chain entropy upon ligand binding is the largest in nSH3:PRM$^{\mathrm{cAbl}}$ (Fig. 4a,b). In the unliganded nSH3, we found that R162 is sandwiched between R160 and R179 (Fig. S9e). In the liganded state, R179 occasionally detaches and points to the negatively charged residues in the RT-loop (Fig. S9e, arrow). This makes R162 more mobile. Among the liganded states, the R160-R162-R179 sandwich was the most preserved in nSH3:PRM$^{\mathrm{NS1B}}$, nearly the same as in the unliganded nSH3 (we measured the sandwich state by the distances between the guanidinium carbon atoms in R160–R162 and R162–R179; Fig. S9e). This is consistent with the negligible side-chain entropy change of R162 in nSH3:PRM$^{\mathrm{NS1B}}$ (Fig. 4b). For nSH3:PRM$^{\mathrm{cAbl}}$, R179 flips less compared to nSH3:PRM$^{\mathrm{NS1A}}$ but the greater R162–E173 H-bond occupancy decrease (Table S1) may have contributed to the larger side-chain entropy increase of R162.

Other than K155, R162, and Y190 explained above, R138 had side-chain entropy increase in all complexes but it is absent in Tables S1–S3. R138 forms H-bond with E188 with greater than 99.9% occupancy in all cases (unliganded and liganded). Hence, its increase in side-chain entropy is not due to breakage of any contact upon ligand binding. A closer examination of surface contacts shows that E188 forms nonpolar contact with L140 (over 98% occupancy in all cases), which in turn forms a nonpolar contact with F141 in the ligand binding pocket of nSH3 Fig. S9f). Note that F141 is one of the two main entropy hotspots of nSH3 that experience the largest side-chain entropy decrease upon ligand binding (Fig. 4). In the nSH3:PRM complex the L140–F141 nonpolar contact occupancy also increases by 14%–18%. Akin to a domino effect, this in turn may have altered the positioning of E188, eventually leading to increase in the side-chain entropy of R138. (Fig. S9f, arrow) We also note that R138–E188 and Y136–Y190 pairs are located at the N- and C-terminal β-sheet of nSH3 (Fig. S9f). This suggests a possibility that the increase in side-chain entropies of R138 and Y190 in the terminal region may have originated from the change in F141 in the ligand-binding pocket. Taken together, side-chain entropy changes in remote residues appear to be caused by propagation of arrangements in lateral contacts between surface residues upon ligand binding. However, since these residues are either charged or polar, changes in surface hydration may also play an important role for the allosteric effect. Further studies are needed to elucidate the robustness of the allosteric information propagation upon ligand binding.

Table S1: Major intra-nSH3 H-bond occupancy differences between unliganded nSH3 and nSH3:PRM$^{\mathrm{cAbl}}$. Only H-bond pairs with average occupancy of the unliganded or the liganded system greater than 50%, and the occupancy difference greater than 10% are shown. Bottom row: per-residue side-chain entropy change upon complex formation (cal/[mol·K]).

	Y136	D142	K155	R162	E173	R179	Y190
Y136	-	-	-	-	-	-	0.165
D142	-	-	-0.377	-	-	-	-
K155	-	-0.377	-	-	-	-	-
R162	-	-	-	-	-0.288	-	-
E173	-	-	-	-0.288	-	-0.127	-
R179	-	-	-	-	-0.127	-	-
Y190	0.165	-	-	-	-	-	-
ΔS_{SC}	0.198	1.139	2.341	2.552	0.703	0.600	0.035

Table S2: Major intra-nSH3 H-bond occupancy differences between unliganded nSH3 and nSH3:PRM$^{\mathrm{NS1A}}$. See Table S1 for explanation.

	Y136	D142	E149	K155	E173	D174	E176	K178	R179	P183	Y186	Y190
Y136	-	-	-	-	-	-	-	-	-	-	-	-0.121
D142	-	-	-	-0.429	-	-	-	-	-	-	-	-
E149	-	-	-	-	-	-	-	-	0.595	-	-	-
K155	-	-0.429	-	-	-	-	-	-	-	-	-	-
E173	-	-	-	-	-	-	-	-	-0.740	-	-	-
D174	-	-	-	-	-	-	0.393	-	-	-	-	-
E176	-	-	-	-	-	0.393	-	-0.700	-	-	-	-
K178	-	-	-	-	-	-	-0.700	-	-	-	-	-
R179	-	-	0.595	-	-0.740	-	-	-	-	-	-	-
P183	-	-	-	-	-	-	-	-	-	-	0.156	-
Y186	-	-	-	-	-	-	-	-	-	0.156	-	-
Y190	-0.121	-	-	-	-	-	-	-	-	-	-	-
ΔS_{SC}	-0.185	0.783	-1.618	2.126	0.841	-2.154	-0.095	0.718	-0.513	-0.754	-0.935	1.931

Table S3: Major intra-nSH3 H-bond occupancy differences between unliganded nSH3 and nSH3:PRM$^{\mathrm{NS1B}}$. See Table S1 for explanation.

	Y136	P183	Y186	Y190
Y136	-	-	-	-0.305
P183	-	-	0.144	-
Y186	-	0.144	-	-
Y190	-0.305	-	-	-
ΔS_{SC}	0.158	-0.708	-1.287	2.573

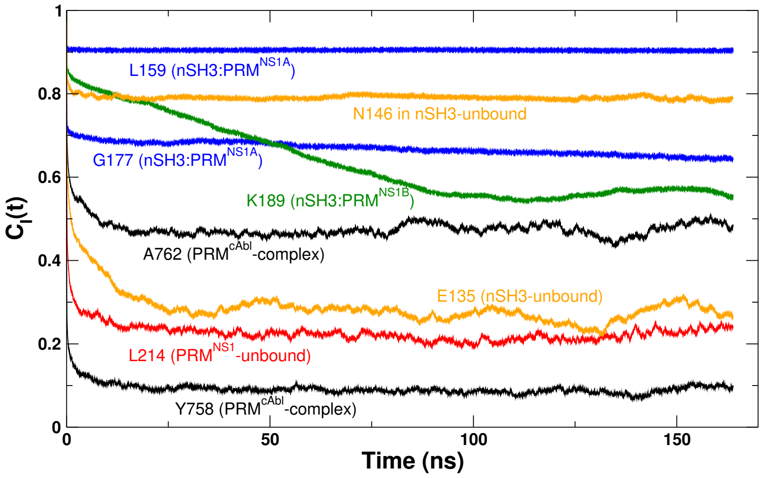

Figure S1: Examples of the angular reorientational correlation function, $C_I(t)$. Residues were selected to illustrate various behaviors (from flexible and rigid domains, and long and short relaxation times). Calculations were done in 0.1-ns increments. After the initial decay, $C_I(t)$ approaches the corresponding order parameter S^2 (Fig. S3).

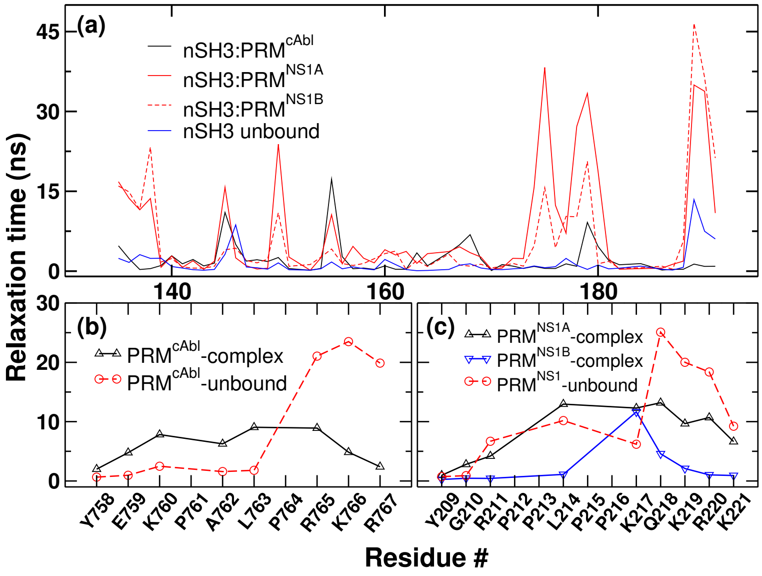

Figure S2: Relaxation times obtained from exponential fits of $C_I(t)$. (a) nSH3 domain in all four models. (b) PRM$^{\mathrm{cAbl}}$ and (c) PRM$^{\mathrm{NS1}}$ in the bound and unbound states.

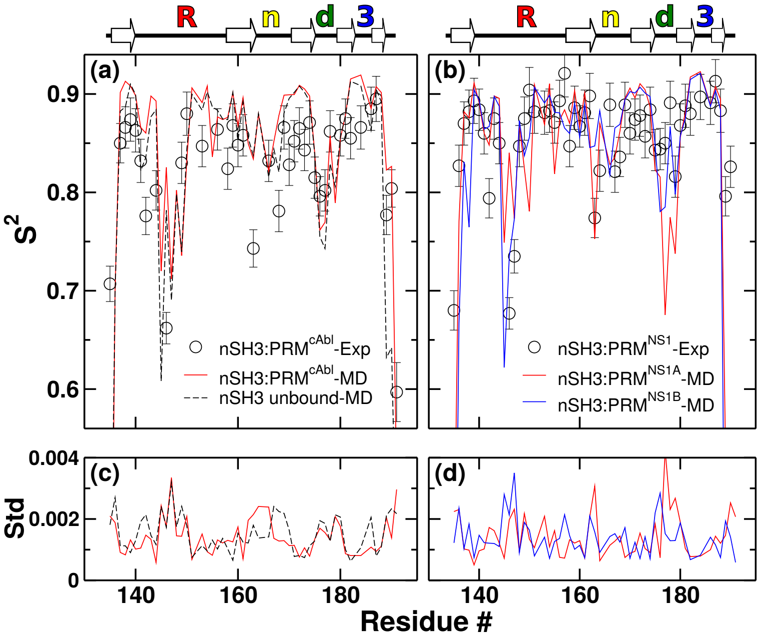

Figure S3: Order parameters (a,b) and the corresponding standard deviations (c,d) for nSH3. Standard deviations of experimental S^2 are given as error bars in panels (a) and (b). (a,c) nSH3:PRM$^{\mathrm{cAbl}}$ and unbound nSH3. (b,d) nSH3:PRM$^{\mathrm{NS1}}$. Circle: experiment; Lines: simulation. Major subdomains (Fig. 1) are marked above each panel, from left to right: RT-loop (“R”), n-Src loop (“n”), distal loop (“d”), and 3_{10} helix (“3”).

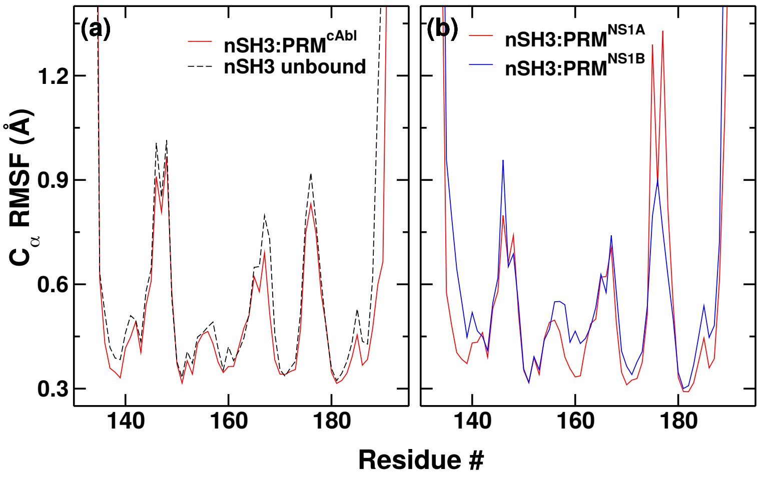

[h]

Figure S4: RMSF of C_α atoms for the nSH3 domain. (a) nSH3:PRM$^{\mathrm{cAbl}}$ and (b) nSH3:PRM$^{\mathrm{NS1}}$.

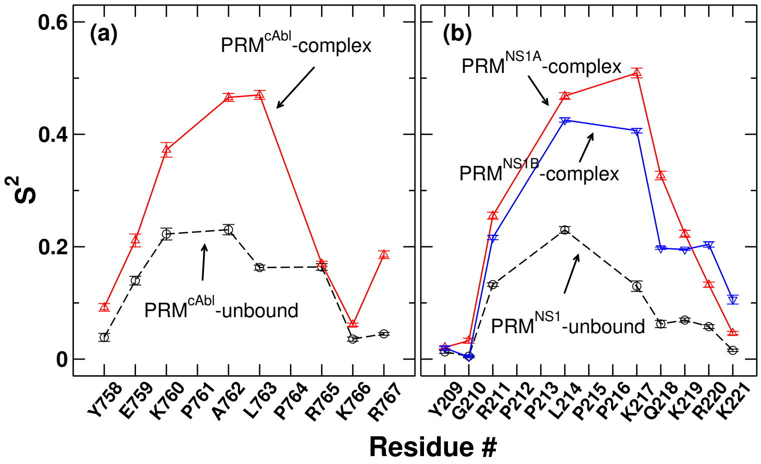

Figure S5: Order parameters of ligands. (a) PRM^{cAbl} and (b) PRM^{NS1}. No order parameter was assigned to proline since it does not have a backbone amide hydrogen atom.

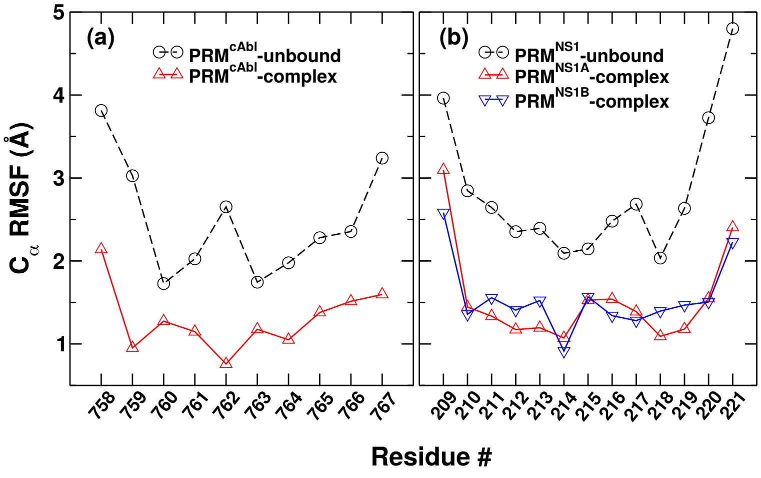

Figure S6: RMSF of C_α atoms for PRMs. (a) nSH3:PRM^{cAbl} and (b) nSH3:PRM^{NS1}.

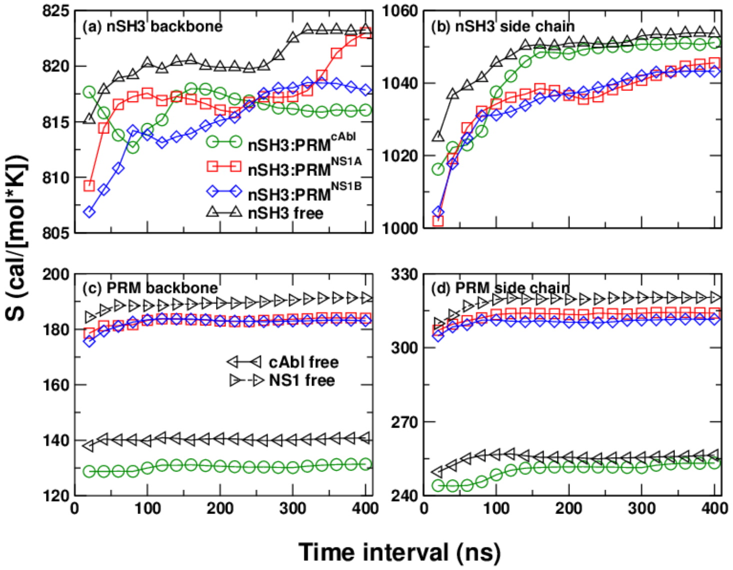

Figure S7: Convergence test using the MIST2 entropy. Horizontal axis is the length of the time interval used for entropy calculation. The first data point used 100–120 ns, the second point used 100–140 ns, *etc.* The last point used the whole 100–500-ns interval. (a) Backbone and (b) side-chain entropy of nSH3. (c) Backbone and (d) side-chain entropy of PRMs. For a given category, the relative difference in entropy between systems involving PRM$^{\text{cAbl}}$ and PRM$^{\text{NS1}}$ is established for time intervals much shorter than 400 ns, except for the backbone entropy of nSH3 where the relative difference starts to emerge for time intervals longer than 300 ns. However, the backbone of nSH3 contributes the least to the entropy change upon ligand binding (Table 1). Since the backbone entropy of nSH3 is similar among different systems, the vertical scale in panel (a) is narrower than those in other panels.

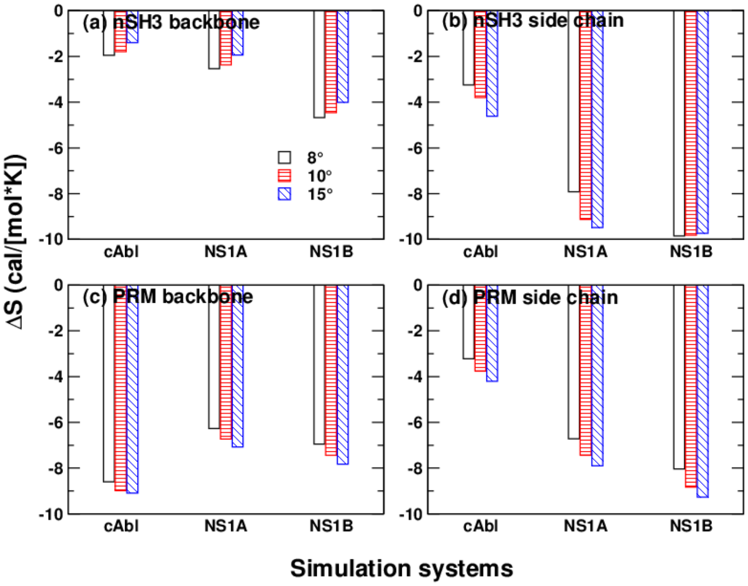

Figure S8: Comparison of MIST3 entropies calculated using different bin size Δ. (a,b) nSH3 and (c,d) PRM. MIST calculations were applied separately for (a,c) the backbone and (b,d) side chains. A larger bin size improves statistics but at the expense of losing information. In an extreme case of a single bin for the entire angular range, PDFs will be identical between the bound and unbound states, so that ΔS will be 0. Thus, reduction in the magnitude of ΔS in the nSH3 backbone (panel a) and to a lesser extent for its side chain in nSH3:PRM$^{\text{NS1B}}$ (panel b) indicates that PDFs for the corresponding angles are relatively narrowly distributed, which is another indicator that nSH3 is stably folded and does not undergo any major conformational change upon PRM binding. Note that relative magnitude of entropies in each panel does not depend on Δ.

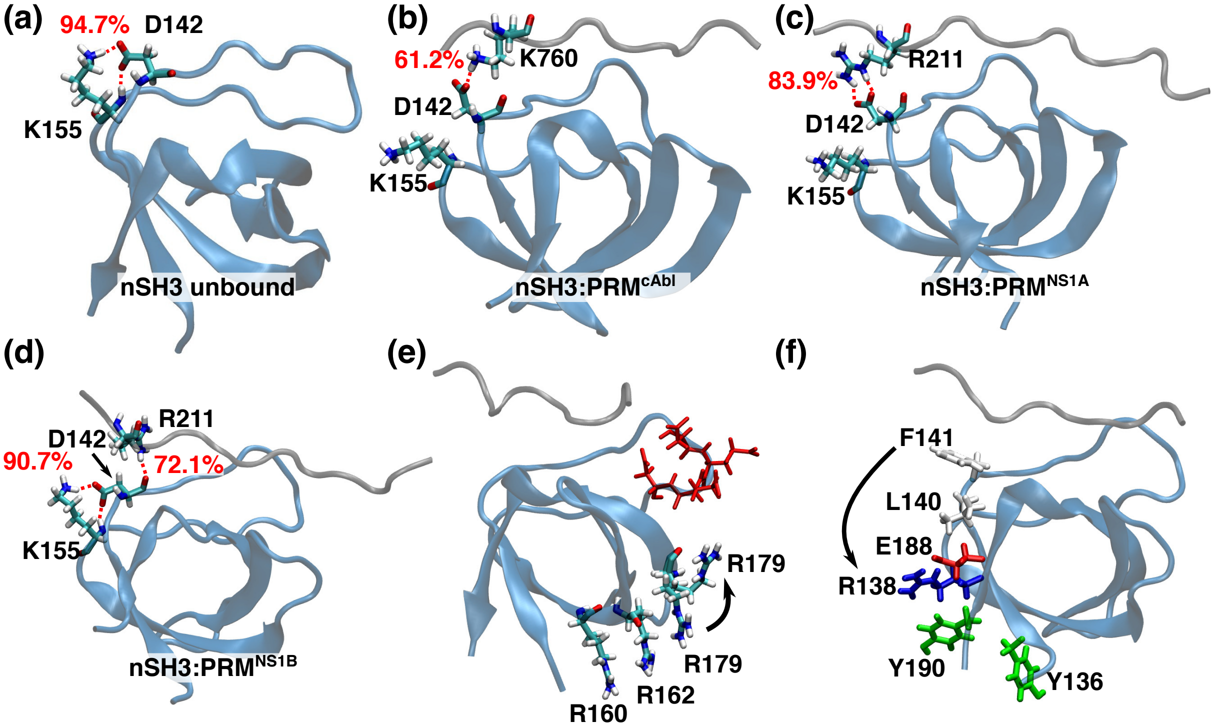

Figure S9: Illustration of the allosteric effect of PRM binding (*cf.*, Fig. 4). Orientations of panels are similar to that of Fig. 4c. (a–d) Increase in side-chain entropy of K155. H-bond (red dashed line) and the corresponding occupancy are shown. Occupancy is residue-to-residue based, regardless of the number of H-bonds between the two. (a) Unliganded nSH3. (b–d) Liganded cases where the K155–D142 H-bond is broken in (b,c). (e) Increase in side-chain entropy of R162. In unliganded nSH3, it is sandwiched between R160 and R179. R179 occasionally flips towards the negatively charged residues in the RT-loop (red sticks), which occurs more often in nSH3:PRM$^{\text{cAbl}}$ and nSH3:PRM$^{\text{NS1A}}$. The distance between the guanidinium carbon atoms of R160 and R162 is 4.20 Å–5.06 Å in all cases. Between R162 and R179, it is 4.89±0.56 Å (unliganded nSH3; avg±std), 5.26±2.11 Å (nSH3:PRM$^{\text{cAbl}}$), 8.23±2.72 Å (nSH3:PRM$^{\text{NS1A}}$), and 4.82±0.62 Å (nSH3:PRM$^{\text{NS1B}}$). In nSH3:PRM$^{\text{cAbl}}$ and nSH3:PRM$^{\text{NS1A}}$ the distance is larger and also fluctuates more. In nSH3:PRM$^{\text{NS1B}}$, the distance is nearly the same as for the unliganded nSH3. (f) Possible pathway of the propagation of changes upon ligand binding, starting from the entropy hotspot F141, to R138 (arrow). The Y136–Y190 pair flanking the R138–E188 pair is also shown, suggesting that ligand binding may have an allosteric effect on the mobility of residues in these terminal β-strands.

SUPPORTING REFERENCES

1. Jarymowycz, V. A., and M. J. Stone, 2006. Fast Time Scale Dynamics of Protein Backbones: NMR Relaxation Methods, Applications, and Functional Consequences. *Chem. Rev.* 106:1624–1671.

2. Maragakis, P., K. Lindorff-Larsen, M. P. Eastwood, R. O. Dror, J. L. Klepeis, I. T. Arkin, M. ø. Jensen, H. Xu, N. Trbovic, R. A. Friesner, A. G. P. III, and D. E. Shaw, 2008. Microsecond Molecular Dynamics Simulation Shows Effect of Slow Loop Dynamics on Backbone Amide Order Parameters of Proteins. *J. Phys. Chem. B.* 112:6155–6158.

3. Chandrasekhar, I., G. Clore, A. Szabo, A. Gronenborn, and B. Brooks, 1992. A 500 ps molecular dynamics simulation study of interleukin-1β in water: Correlation with nuclear magnetic resonance spectroscopy and crystallography. *J. Mol. Biol.* 226:239–250.

4. Bhatt, V. S., D. Zeng, I. Krieger, J. C. Sacchettini, and J.-H. Cho, 2016. Binding Mechanism of the N-Terminal SH3 Domain of CrkII and Proline-Rich Motifs in cAbl. *Biophys. J.* 110:2630–2641.

5. Shen, Q., J. Shi, D. Zeng, B. Zhao, P. Li, W. Hwang, and J.-H. Cho, 2018. Molecular Mechanisms of Tight Binding through Fuzzy Interactions. *Biophys. J.* 114:1313–1320.

6. Kay, B., M. Williamson, and M. Sudol, 2000. The importance of being proline: the interaction of proline-rich motifs in signaling proteins with their cognate domains. *FASEB J.* 14:231–241.